Extending the operating limits and performances of centimetre-scale wind turbines through biomimicry

Aurélien Carré, Pierre Gasnier, Émile Roux, Laurent Tabourot

Applied Energy 326 (2022) 119996

Contents lists available at ScienceDirect

Applied Energy

journal homepage: www.elsevier.com/locate/apenergy

Extending the operating limits and performances of centimetre-scale wind turbines through biomimicry

Aurélien Carré [a,*], Pierre Gasnier [b], Émile Roux [a], Laurent Tabourot [a]

[a] Université Savoie Mont Blanc, SYMME, F-74000 Annecy, France
[b] Université Grenoble Alpes, CEA-LETI, MINATEC, F-38000 Grenoble, France

GRAPHICAL ABSTRACT

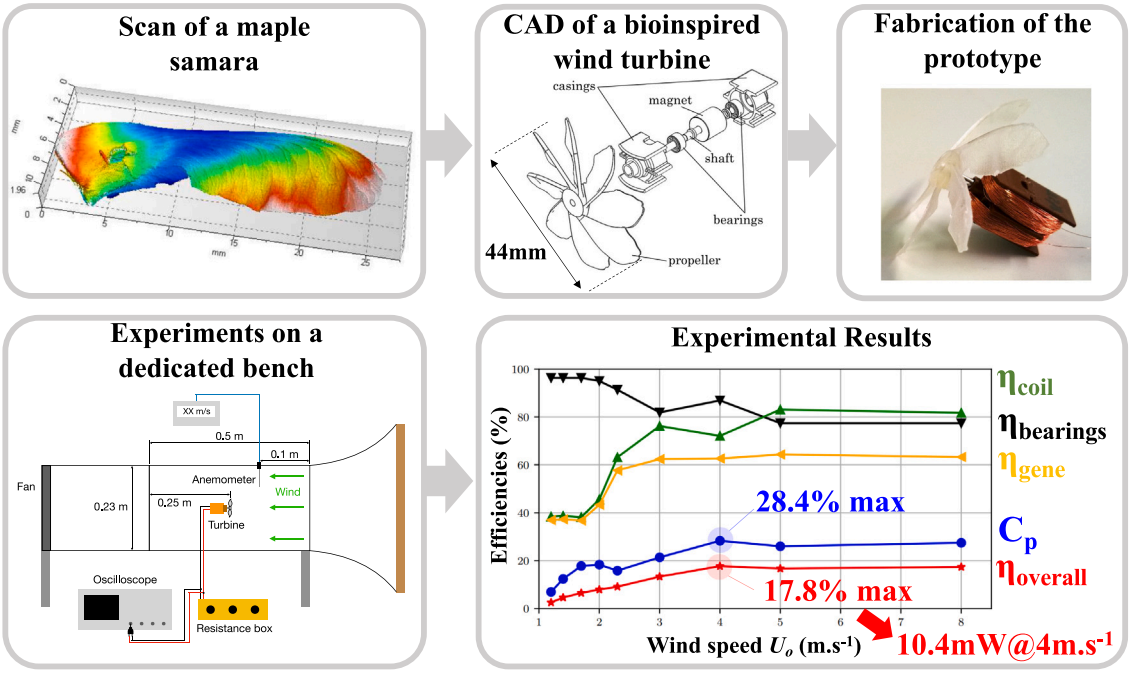

ARTICLE INFO

Keywords:
Biomimetics
Wind turbine
Centimetre-scale
Energy harvesting
Low wind speeds

ABSTRACT

This paper reports the design and fabrication of an innovative small-size propeller and its experimental testing once assembled with an electromagnetic generator. The bioinspired rotor is based on the shape and behaviour of maple samaras that optimise the aerodynamics at low Reynolds numbers. To the authors' knowledge, it is the first samara-based wind energy harvester reported to date and one of the smallest wind turbines in the literature. The different blade angles and the number of propeller blades are optimised. A permanent magnet miniature generator with low friction ceramic bearings is used to convert rotation into electrical power. The performance of this 44 mm diameter horizontal-axis wind turbine is tested under wind speeds from 1.2 to 8 m s^{-1}. The output electrical power measured in resistive load is between 41 μW and 81.7 mW, which leads

* Corresponding author.
E-mail address: aurelien.carre@univ-smb.fr (A. Carré).

https://doi.org/10.1016/j.apenergy.2022.119996
Received 8 June 2022; Received in revised form 21 August 2022; Accepted 14 September 2022
Available online 27 September 2022

to an overall efficiency between 2.6 (1.2 m s^{-1}) and 17.8% (4 m s^{-1}). Estimates of different losses in the harvester make it possible to determine power coefficient C_P which reaches 28.4%. Among the miniature wind turbines in the literature, this device demonstrates one of the highest rates in terms of efficiency and power density. Moreover, thanks to its operating speed decreased to 1.2 m s^{-1} – the lowest in the state of the art – it presents one of the largest ranges of airspeeds for energy harvesting.

Table 1
Different energy sources with their available power density [1].

Energy source	Power density
Solar (outside)	15 000 μW cm^{-2}
Airflow (@ 5 m s^{-1})	7 500 μW cm^{-2}
Solar (inside)	100 μW cm^{-2}
Vibrations	100 μW cm^{-3}
Airflow (@ 1 m s^{-1})	60 μW cm^{-2}
Thermal gradients (10 °C)	15 μW cm^{-3}
Lithium batteries	45 μW cm^{-3}
Rechargeable lithium batteries	7 μW cm^{-3}

1. Introduction

As the spread of Wireless Sensor Nodes (WSNs) accelerates, the need for electrical power will grow and may become problematic in the years to come. These sensors are used for a wide range of measures – temperature, humidity, presence, vibrations, etc. – and are usually powered by batteries. In the actual context of climate change, they could for example make it possible to observe the effects of rising temperatures and other parameters almost anywhere on the planet. Their operation requires periodical maintenance with inevitable costs, especially if the WSN is located in a difficult-to-access area. In order to avoid it, some developments are now made in the field of energy harvesting with Micro Electro-Mechanical Systems (MEMS). Energy harvesting is the principle of extracting energy from different ambient sources – vibrations, light, water or airflows, etc. – and converting it into electricity; in most cases to power electronic components. A brief comparison of power densities was made by Huet in 2016 and is reported in Table 1. Compared to batteries, airflows appear to be interesting, even at low wind speeds (down to 1 m s^{-1}). It can also be used as a complement to solar power which is very intermittent.

To give an order of magnitude of the power required by a WSN, Huet also studied a standard platform from Texas Instruments (model ez430-RF2500), which is also a case study in [2]. It includes a low-power microprocessor and a 2.4 GHz radio module. The power consumption of this platform in sleep mode is around 2.3 μW, during transmission 82 mW and during reception 75 mW. An external 320 μW accelerometer is plugged in [1]. The results show that this node could run its measure and transmission procedure every 5.3 s with an input power of only 100 μW. This shows that a centimetre-scale wind harvester, exploiting very low airflows, could be enough to supply a complete WSN.

Airflow-driven energy harvesters exploit the power of the air, which is expressed as:

$$P_{air} = \frac{1}{2}\rho S U_0^3, \tag{1}$$

with $\rho = 1.185$ kg m^{-3} the air density, S the system cross-section, and U_0 the airspeed upstream of the system. For horizontal-axis wind turbines, because of the Betz limit, no more than 16/27 ($\sim 59\%$) of this power is actually convertible into mechanical power on the harvester shaft. This law thus limits the propeller's aerodynamic efficiency, with a power coefficient C_P ($C_P < 0.59$). On top of that, the generator has its own mechanical to electrical conversion efficiency, that can be noted η_{gene}. Finally, the output electrical power is:

$$P_{elec} = \eta_{gene}.C_P.P_{air} = \eta.P_{air}, \tag{2}$$

with η the overall efficiency of the harvester.

Since the aim is to power a WSN, the wind turbine has to be miniaturised. This process impacts mainly the power coefficient of the propeller and consequently the overall efficiency. Overall efficiency goes down to around 30%–40% for rotor diameters between 1 and 4 m [3–5], to 20% for 40 cm with some optimisations [6–9], with the smallest system being a 7.5 mm turbine working at very high wind speeds and presenting the worst efficiency of less than 0.4% [10]. One way to improve small turbine performance is to add a duct around the rotor: the power production can be increased by 2.68 on a 12.8 cm diameter wind turbine [11], by 2 on a 18 cm one experimentally, and even by 3.64 numerically with an optimised duct [12]. Lipian et al. also recently conducted a numerical study on a 32 cm diameter rotor, focusing on the effect of adding a second rotor just behind the first on their aerodynamical properties [13]. However, this solution presents a more complex structure and a larger outer volume. In the present context of intense urbanisation, increased energy needs and the development of smart cities, Dar et al. investigated on a scaled-down roof-mounted wind turbine [14]. On a flat terrain, the three-bladed 10.5 cm diameter turbine presents a maximal power coefficient of 34%. The authors then showed that for a same rotational speed of the rotor, the geometry of the model building, where is mounted the turbine, has an influence on the power production.

The work in the present paper focuses on miniature wind turbines, with rotor diameters of a few centimetres (7 cm and below), working at relatively low airspeeds (less than 10 m s^{-1}). In addition, only the generators using electromagnetic conversion will be taken into account, as it is the technology used in this study and presents an interesting power density at small dimensions compared to the electrostatic conversion [15]. The following state of the art presents this type of devices.

In 2016, Marin et al. developed a wind turbine with a rotor diameter of 7.2 cm [16]. The output AC power is from 2.58 to 270.85 mW for a wind speed U_0 from 2 to 11 m s^{-1}. These results lead to an overall efficiency η of 15% at its maximum. A few years before, an Italian research team specifically studied the electronic extraction circuit and the optimal resistive load of a 6.3 cm diameter, four-blade wind turbine [17]. The harvester produces an electric output power of 2 mW at 2.4 m s^{-1}, giving $\eta = 3\%$, and 10 mW at 4.6 m s^{-1}, giving $\eta = 6\%$. Very recently, Kim et al. studied the impact of a duct and wind direction on a 4.5 cm-diameter wind turbine [18]. For speeds between 5 and 10 m s^{-1}, the efficiency is situated between 3 and 8% with output powers from 3.7 to 69.9 mW. In 2007, Rancourt et al. compared three existing commercial propellers with a diameter of 4.2 cm [19]. Amongst the three, the pitch angle varies along the blades and at the tip. An existing generator is also used and its load is changed from open- to closed-circuit. For one propeller, generated power is calculated at 2.4 to 130 mW for wind speeds from 5.5 to 11.8 m s^{-1}, respectively. The resulting overall efficiency of the miniature windmill is from 1.5 to 9.5%, with a generator efficiency that does not exceed 53%. The other two rotors show a power coefficient of around 25%, which is a good result for the size, but the electrical powers are not evaluated.

The French team of Gasnier et al. recently made two prototypes: a 3.5 cm diameter in 2019 and a 3.45 cm in 2018 [20,21]. Their cut-in speeds are 2 and 2.5 m s^{-1}, respectively. They are both tested shrouded and the first one is also tested without the shroud. This one presents the highest performances without its shroud with an interesting maximal end-to-end efficiency of 28%; but this value drops down to 10 to 12% for the lowest and the highest airflows tested. The harvesters output

Table 2
Overview of the maximum efficiencies of existing harvesters.

Reference	Rotor diameter	Maximal efficiency	Maximal electrical power
[16]	7.2 cm	13.4%	270.85 mW @ 11 m s^{-1}
[17]	6.3 cm	8%	9.95 mW @ 4.7 m s^{-1}
[18]	4.5 cm	8%	69.9 mW @ 10 m s^{-1}
[19]	4.2 cm	9.6%	130 mW @ 11.8 m s^{-1}
[20]	3.5 cm	28%	24.6 mW @ 7 m s^{-1}
[21]	3.45 cm	12%	4.5 mW @ 4 m s^{-1}
[22]	2.6 cm	3.2%	5.7 mW @ 8.8 m s^{-1}
[23]	2 cm	3.9%	4.32 mW @ 10 m s^{-1}
This work	4.4 cm	17.8%	81.7 mW @ 8 m s^{-1}

200 μW at 1.5 m s^{-1} and 24.6 mW at 7 m s^{-1} (for [20]) and 350 μW at 2 m s^{-1} and 4.5 mW at 4 m s^{-1} (for [21]). One of the smallest harvesters created is a 2.6 cm diameter swirl type turbine by Zakaria et al. [22]. It delivers a power that varies between around 450 μW and 5.7 mW but for higher airflows — between 3.9 and 8.8 m s^{-1}. The best overall efficiency is quite low at 3.2%. Finally, with a rotor diameter of 2 cm and a shroud diameter of 3.2 cm, the prototype developed by Howey et al. in 2011 is the smallest that works at low wind speeds [23]. As long as the Reynolds number never exceeds 2000, a NACA4402 profile is used for the blades based on data generated by Kunz et al. [24]. The number of blades can be changed (3, 6, or 12) and is set at 12 for optimal performance. To convert mechanical rotation into electrical power, the authors chose to insert small NdFeB magnets in two rotating outer rings that interact with a fixed stator coil. This solution frees up space in the rotor area. The electrical output power is 80 μW at 3 m s^{-1} and 4.32 mW at 10 m s^{-1}; the maximal power coefficient C_P is 9% and the maximal overall efficiency of the harvester is 3.9%.

In order to summarise the above characteristics, the maximal overall efficiency η for each device and for the prototype of this study are listed in Table 2, as well as the maximal output electrical power.

Finally, the prototypes of the literature highlight the main issue in the process of extreme miniaturisation: about 13% at most of the wind power is actually converted into electricity. A great part of the input power is therefore lost at different stages of the turbine. The problem is that with such a low efficiency and at a centimetre scale, a harvester could not exploit low wind speeds because it would not exhibit a sufficient power to supply a WSN. Moreover, the lowest operating speed is 1.5 m s^{-1} for a diameter of 3.5 cm, which must be improved to exploit even lower wind speeds. In parallel, the highest working speed could be increased, in order to have the widest possible range of wind speeds.

The small efficiencies observed can be explained by the low Reynolds numbers close to the rotor blades. This number is given by:

$$Re = \frac{V c}{\nu}, \tag{3}$$

with V the relative airspeed arriving on the blade, c the blade chord, and ν the kinematic viscosity of the air. In the case of centimetre-scale harvesters, c and V are very small, giving Re around $10^3 - 10^4$, which characterises a laminar (or low turbulent) flow [23]. As a consequence, the lift-to-drag ratio of the blades is way beyond the ones seen on large scale, giving a less efficient wind turbine [3]. One of the main challenges of miniaturisation is to find new blade designs with better aerodynamic properties, in order to optimise the propeller's power coefficient and thus the harvester's overall efficiency.

In this goal, Kunz showed that the use of thin and cambered profiles (as the NACA4402 one first chosen by Howey) could increase the lift-to-drag ratio, at small scale and low Reynolds numbers (as low as 1000) [24]. Another study by Sunada et al. gives the same conclusions about the positive influence of the camber, with hydrodynamic tests [25]. The existing small-scale harvesters use this classic type of blade design. Then, is there another more efficient way to improve centimetre-scale propellers' performances ?

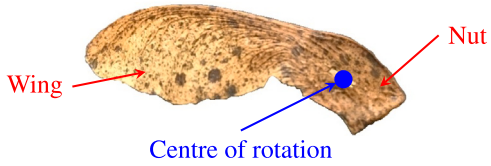

Fig. 1. Two main parts of a maple samara.

In this study, we chose to follow a more innovative method which is often used in energy harvesting: biomimicry. Experimentations have been made to improve wind turbine performances thanks to this method. For example, tubercles on whales' flippers improve performance and manoeuvrability, and delay stall [26,27]. Based on that, it has been shown that at Reynolds numbers around 10^5, blades with leading-edge tubercles demonstrate enhanced performance [28]. Other studies use the shape of owl wings in order to reduce drag force and noise on a static wing [29], or of bird wings on a 1 m diameter wind turbine to get a better C_P [30]. The use of bioinspired flexible blades on small wind turbines is also promising: an increase up to 35% of the output power can be achieved on a 30 cm diameter wind turbine [31], and at a smaller scale, it was recently shown that it can improve the harvester properties (lower cut-in speed, passive modification of the blade angles, shorter time to achieve maximum voltage etc.) [32]. For the purpose of the present study, the maple seed specimen seems very interesting: the Reynolds number of their wings during their rotation is found to be in the range of 10^3–10^4 [33–36], which corresponds well with centimetre-scale turbines. An investigation by Holden et al. in 2015 provides some good leads on what could be useful for the issue presented here [37]. Indeed, the rotation of a maple seed under a wind flow is numerically studied to evaluate its mechanical efficiency. The results show a power coefficient C_P of 59%, very close to the physical Betz limit of 59.3%. This result has to be completed by experimental testing: in our work, we then characterise maple seed horizontal rotation in a real wind tunnel. This gives good hope that by copying maple seed design, turbine blades could get better aerodynamic properties and so turbine propellers could increase their power coefficient.

Some details of the design process and preliminary performance data were reported previously in [38]. In the present paper, we present maple seed behaviour in detail and the reverse engineering process of a blade in Section 2. Propeller fabrication is described in Section 3 and additional performance results in Section 4 for a more complete characterisation of the harvester. Bearing loss measurements are also made, allowing an estimation of the power coefficient.

2. Maple seeds bioinspired design of the blades

In the entire animal and vegetable kingdom, the only specimen that has the same movement as a horizontal axis wind turbine is the maple seed, also called samara. As reported above, their mechanical efficiency in rotation appears to reach the maximum achievable level.

2.1. Samaras free fall

The total length of samaras can be several centimetres long, with some species that can be as small as 1 cm [39]. They are composed of two parts: one heavier part that is the dry fruit or nut, and another one much lighter that is the wing (Fig. 1). For the Norway maple (or *Acer platanoides*) studied here, which is the most common in Europe and the most studied, mass distribution was investigated for eight seeds with lengths between 28 and 35 mm. For this purpose, each seed was weighed, then the wing was separated from the nut. It appears that the nut represents on average 79.7% of the total mass.

When a samara falls from a tree, this mass distribution between the two different parts allows it to autorotate and glide away from the tree,

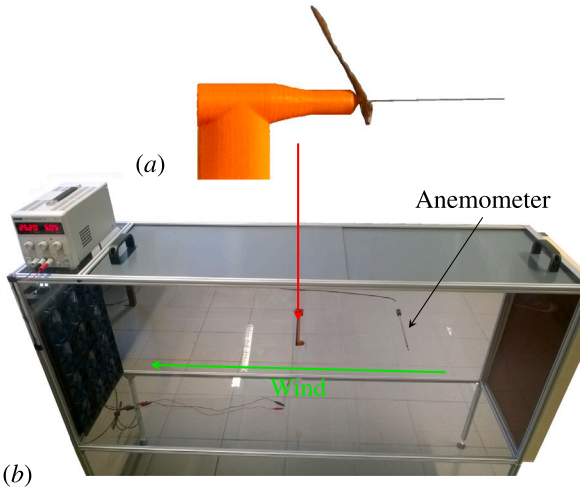

Fig. 2. (*a*) Plastic support with the 0.5 mm diameter rod and a samara placed on it, and (*b*) low speed wind tunnel for experiments.

which favours seed dispersal [40,41]. Depending on the species, this rotation is measured to be between 760 and 1430 rpm (or between 80 and 150 rad s^{-1}), and the vertical speed around 1 m s^{-1} [39,42]. Interestingly, as well as the Reynolds number, these parameters are in the same order of magnitude as the ones observed for the operating conditions of centimetre-scale wind harvesters at low wind speeds [20].

The difference remaining between samaras and turbine propellers is the position of the centre of rotation. Indeed, for samaras, it is proven that the instantaneous centre of rotation follows a helical trajectory [36,39]: brought back in a perpendicular plane, it is thus not fixed but moves in a circle. This is why additional experiments are conducted where the centre of rotation is forced to be immobile.

2.2. Rotation on a fixed axis with natural blade

2.2.1. Experimental setup

Here, the constrained motion of maple seeds is investigated in order to get closer to turbine blade motion and to determine if, in this configuration, they are as efficient as during a free fall.

For these tests, five samaras are drilled in the centre of their nut and placed on a thin rod to create an artificial centre of rotation. Their wingspan (from the hole to the wing tip) is comprised between 20 and 31 mm to have some disparity within the specimens. The rod is glued to a plastic part to block samara translation (Fig. 2(*a*)). This support is then set in a wind conduct where airflow is applied to the samaras, while their rotation speed is measured with a highspeed camera outside of the conduct (the time needed for one revolution is deduced from the camera frame rate of 2000 fps). For the purpose of this study, a low speed wind tunnel was built: indeed, stabilised airspeed has to be as low as the samaras' fall speed, i.e., around 1 m s^{-1}. This tunnel is also used to characterise the harvester prototype in a subsequent section. Its cross sectional area is 400 × 600 mm^2, with a length of 1.5 m. A honeycomb plate is placed on one end and several fans on the other end. It generates wind speeds between 0 and 2.3 m s^{-1}, which are measured by a hot wire anemometer (TSI 8465-300) with a precision of ±0.01 m s^{-1} (Fig. 2(*b*)).

Along the 400 mm side and at the location of the samaras support (0.75 m from the tunnel entrance), the evolution of wind speed is measured for an applied constant wind of 1 m s^{-1} (Fig. 3). It shows that there are 100 mm boundary layers close to the walls where the wind speed is smaller than the one measured by the anemometer. This leaves a 200 mm width for the experiments, which is enough regarding the wingspan of samaras and the target dimensions for the prototypes (diameter ≤ 7 cm).

Table 3
Rotation speeds for samaras with fixed axis (mean value ± standard deviation).

	Rotation speed (rpm)	
Free fall [43]	777 ± 264	
This work	Measure 1	Measure 2
Samara 1	1442 ± 37	1337 ± 54
Samara 2	1690± 50	1738± 51
Samara 3	1337± 23	1356± 24
Samara 4	1576± 39	1557± 10
Samara 5	1814± 16	1843± 11

It is also calculated that the swept disk area of the samara during its rotation is only 1% of the tunnel area.

2.2.2. Rotation speeds

As a reference, we used data from a 2021 study with 30 specimens of the Norway maple species [43]. Nave et al. measures the rotation speed of samaras in free fall at 777 ± 264 rpm (81.4 ± 27.6 rad s^{-1}). Moreover, descent speed is measured between 1.03 and 1.1 ± 0.32 m s^{-1}.

For our experiments, the wind speed in the tunnel is thus set to 1 m s^{-1} to have the same relative airspeed on the samaras. Among the five seeds, the direction of rotation could be different: here, as the sign of the rotation speed value is not interesting, the absolute value is given. Each speed is measured on a few revolutions and during two tests, to obtain information on repeatability. The results are detailed in Table 3.

The comparison between free falls and constrained motion reveals that with their axis of rotation fixed, the Norway maple samaras always have higher rotation speeds. The increase ranges from 72% to 137% and leads to values that are commonly observed on miniature-turbine propellers. This suggests that samaras could have really interesting aerodynamic properties as centimetre-scale blades.

To get the best model for the design, samara 5 is chosen as it demonstrates the highest rotation speed with a fixed axis. The aim is thus to copy its shape, with the highest possible precision.

2.3. Reverse engineering

One face of samara 5 is scanned with an Altimet AltiSurf©520 in order to obtain the coordinates of about 3 000 000 points. Vertical resolution is 0.03 µm and in the plane resolution is 10 µm. The mapping of these points is given in Fig. 4. The hole in the nut for the experiments with constrained rotation is visible.

Thanks to the high resolution, the details of the structure appear clearly, in particular the wing undulation on the trailing edge and the veins on the wing. This last characteristic is known to have a great influence on the aerodynamic properties [44,45]. Unfortunately, the height of the veins is less than 0.05 mm. Thus, they cannot be reconstructed correctly on a CAD software: the design has to be simplified.

The thickness of different parts of the seed – nut, leading edge, wing – are also measured. Then, the samara is built by CAD with the outer contour from the scan. A view from one side of the reconstructed model is proposed in Fig. 5(*a*). Fig. 5(*b*) shows a section of the wing: the leading edge can be seen on the right with a more important thickness than the trailing edge. The wing profile is replicated as close as possible thanks to the different measurements.

In order to obtain turbine blades, the zone corresponding to the nut of 4 mm radius is removed from the samara CAD model, leaving only the wing (Fig. 5(*c*)).

One can notice that the wing is thicker on the blade than on the samara. Indeed, because of the chosen fabrication process – additive manufacturing with plastic resin – the real dimension of 0.1 mm is not practically achievable. The wing is therefore thickened to guarantee quality fabrication but remains as thin as possible; the minimum thickness value here is 0.4 mm. As a consequence, the leading edge of the blade is also modified and a final thickness of 1 mm, for an initial value of 0.5 mm is obtained.

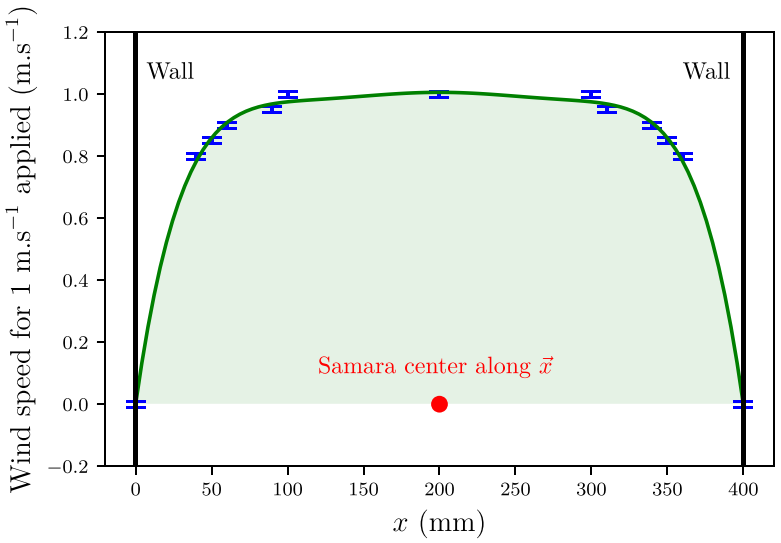

Fig. 3. Evolution of the wind speed in the tunnel to highlight boundary layers.

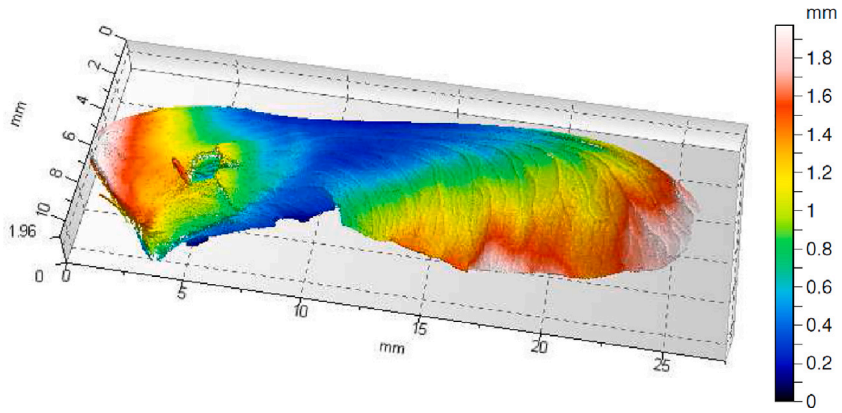

Fig. 4. Scan of the samara with colours representing the height of the points.

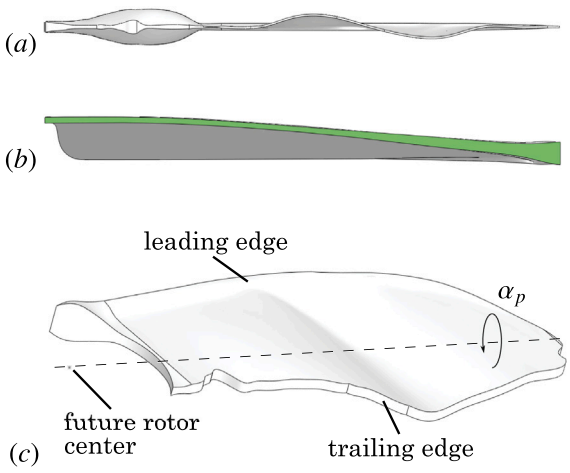

Fig. 5. CAD reconstruction of a bioinspired blade for the propeller: (*a*) view of wing undulation on the trailing edge, (*b*) view of a section of the wing, and (*c*) global view.

3. Fabrication of the propeller

3.1. 3D printing

To create the bioinspired propeller, several wings are linked to an 8 mm diameter hub – corresponding to the size of the removed nut –, which has a 1.8 mm hole to join with the generator. Two angles of the blade can be changed: pitch angle (noted α_p) and coning angle (noted β). Pitch angle is induced by the blade rotation on itself – and thus impacts its angle of attack with the relative wind – and is represented on the blade in Fig. 5(*c*). It should be noted that this angle is constant from the root to the tip of the blade. The coning angle is the one between the propeller's rotation plane and the blade axis; it is an angle that appears during samara autorotation.

The number of blades can vary; propellers with 4, 6, and 8 blades were studied. The pitch angles tested are 8, 20, 30, 40 and 50°, in order to have a great variety of results without testing too much propellers. The coning angles are 5, 10 and 15° as these values are similar to the ones observed on samaras with fixed axis. Consequently, depending on the coning angle, propeller diameter is 44.4, 43.9 or 43.1 mm, respectively.

For propeller fabrication, complex machining and moulding processes were discarded because of the complexity of implementing this type of thin part. Therefore, a rapid prototyping process consisting

Fig. 6. Example of a propeller after fabrication, with imperfections due to the links with the supports.

Table 4
Summary of the bioinspired propellers and harvester specifications.

Specification	Value
Rotor diameter	4.31, 4.39, 4.44 cm
Hub diameter	0.8 cm
Rotor area	15.2 cm^2
Number of blades N_b	4, 6, 8
Pitch angle α_p	8, 20, 30, 40, 50°
Coning angle β	5, 10, 15°
Generator area	1.2 cm^2
Generator resistance R_{in}	84.5 Ω
Harvester outer volume	38 cm^3

in plastic resin photopolymerisation, or stereolithography (SLA), was chosen. This technique is chosen mostly thanks to its resolution of fabrication: with the Formlabs Form 2 used, the laser beam has a diameter of 140 µm, and layer thickness is 25 µm. However, as it is discussed in the previous section, this resolution is not sufficient to create the parts with the original dimensions of the samara.

In the SLA process, the manufactured part is maintained with supports that are printed at the same time as the propeller. Those supports have to be removed after the drying step to get the final part, which can be delicate with fragile structures as thin blades. Fig. 6 shows a four blades propeller with imperfections coming from the supports and the removal step.

3.2. Prototype construction

The generator used for this prototype is a homemade coreless, permanent-magnet, micro-machine. This technology shows a low starting torque, which is interesting as it enables propeller rotation in low wind speeds. The magnet is a 7.5 mm diameter cylinder with a length of 7.5 mm and a 1.98 mm hole. It is made of samarium-cobalt (SmCo); this alloy presents one of the best remanent inductions (around 0.9 T) and thus can create a high current in the coil. It is press-fit onto the generator shaft, which has a 2 mm diameter and a length of 22.3 mm. This rotating shaft is supported by two inner and outer, 2 and 5 mm diameter micro-ceramic bearings selected for their low friction. This assembly is contained in a plastic casing made in two parts. Then, a 63 µm diameter copper wire is wrapped several hundred turns around the casing. The outer dimensions of this miniature generator are 14 × 11 × 25 mm^3, and its internal resistance R_{in} is measured at 84.5 Ω. Finally, the propeller is also press-fit onto the outer end of the shaft. Table 4 summarises those specifications and Fig. 7 shows the different parts in an exploded view of the harvester CAD with one of the propellers, as well as one of the real prototypes.

4. Testing and results

4.1. Experimental setup

For the experimental testing of the harvester, the wind tunnel built to study samaras is used for low speeds, from 0 to 2.3 m s^{-1}. In addition, in order to characterise the prototype on a larger band of airflows, another existing tunnel is used for higher speeds, between 3 and 8 m s^{-1}. This tunnel can create winds between 3 and 45 m s^{-1}. The cross-section of the vein is 23 × 23 cm^2 and 50 cm long. Schematics of the two wind tunnels are represented in Fig. 8. The hot wire anemometer is positioned in both tunnels and a test at 2.3 m s^{-1} is performed to confirm that the results are equivalent. For the two duct sections, a verification that the rotor cross-sectional area does not obstruct more than 3% of the tunnel is performed to guarantee good flow quality.

The copper wire of the electromechanical generator is directly connected to a resistive load with a variable value R_{load}: the electrical power produced by the harvester will be entirely dissipated in it by heating. For the tests, its value varies from 5 Ω to 90 kΩ. To measure the alternative voltage created, an oscilloscope with an impedance of 1 MΩ is connected in parallel to the resistor. This impedance gives an equivalent resistive load R_{eq} connected to the generator that will range from 5 Ω to 82.6 kΩ.

According to Joule's law, the power dissipated in the load can therefore be expressed as:

$$P_{elec} = R_{eq} I^2 = \frac{U_{RMS}^2}{R_{eq}}, \tag{4}$$

with I the current in the circuit and U_{RMS} the root mean square voltage measured by the oscilloscope.

4.2. Uncertainty analysis

The relative measurement error on the output voltage is $\frac{\Delta U_{RMS}}{U_{RMS}} = 1\%$ and the one on the resistive load is $\frac{\Delta R_{eq}}{R_{eq}} = 1\%$. The method to determine the uncertainty of a function with multiple independent variables is reported in [12]. Then, from (4), it is possible to express the relative measurement error on the output electrical power:

$$\frac{\Delta P_{elec}}{P_{elec}} = \sqrt{\left(2\frac{\Delta U_{RMS}}{U_{RMS}}\right)^2 + \left(\frac{\Delta R_{eq}}{R_{eq}}\right)^2} \tag{5}$$

This gives a relative error for P_{elec} of 2%.

4.3. Estimates of losses

As stated in the introduction and in (2), different losses appear in the wind turbine between the raw wind power P_{air} and the harvested power P_{elec}. First, the power coefficient C_P takes place between the air power and the mechanical power on the rotor shaft P_{meca}. Then, a loss of power due to friction noted P_b appears in the bearings. Finally, the generator coil is also subject to heating through its internal resistance, which creates the Joule losses noted $P_{coil,J}$ and eddy current losses noted $P_{coil,E}$. In order to summarise those different losses and the efficiencies in the harvester, a diagram is proposed in Fig. 9. This section explains how these three losses are calculated.

4.3.1. In the coil

On one hand – as stated in [20] or [23] –, R_{in} resistance losses due to Joule effect in the generator are given by:

$$P_{coil,J} = R_{in} I^2 = R_{in}\left(\frac{U_{RMS}}{R_{eq}}\right)^2 \tag{6}$$

It is possible to express it as a function of the electrical power in the resistive load, as they are crossed by the same current:

$$P_{coil,J} = \frac{R_{in}}{R_{eq}} P_{elec} \tag{7}$$

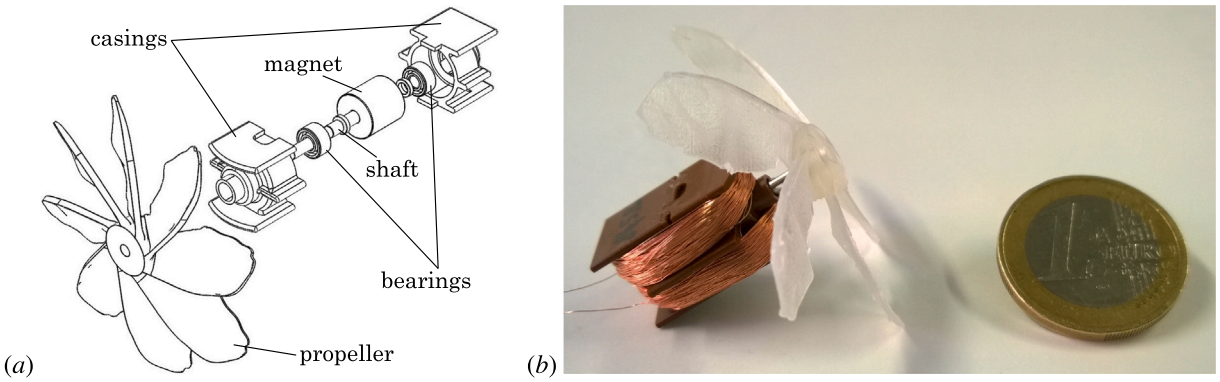

Fig. 7. The bioinspired harvester: (*a*) CAD exploded representation (N_b = 8) and (*b*) real prototype (N_b = 6) next to a 1€ coin for scale.

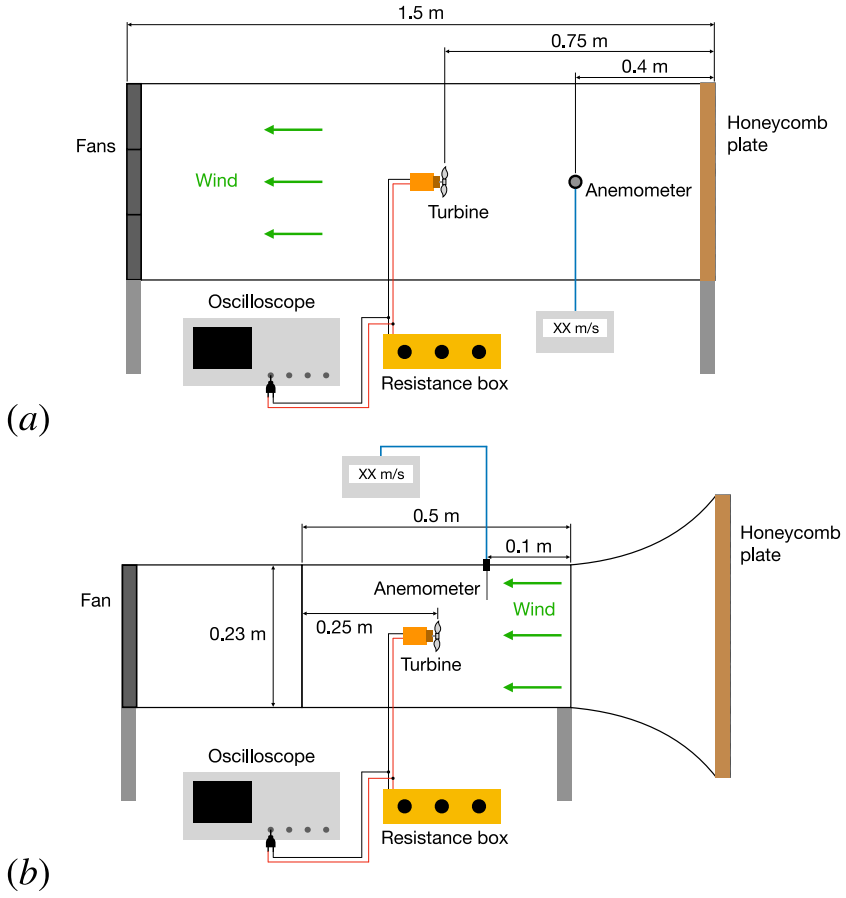

Fig. 8. Schematics of (*a*) the first and (*b*) the second wind tunnel used for the experiments, with dimensions.

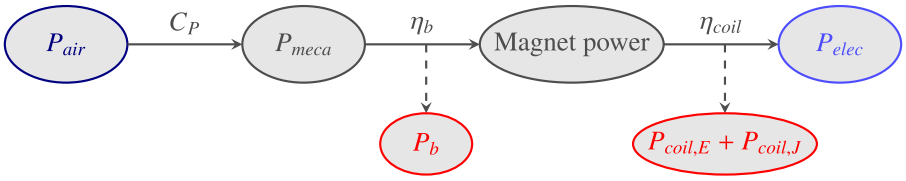

Fig. 9. Powers, losses, and efficiencies at different harvester stages.

Thus, for the values of R_{eq} close to R_{in}, coil losses will be of the same order as harvested power; it will even be larger when $R_{eq} < R_{in}$. Consequently, to obtain an interesting generator efficiency, R_{eq} has to be as high as possible.

On the other hand, there is no proper study on eddy current losses at a centimetre scale in permanent magnet generators. Then, from results on larger machines, those losses are assumed to be 1% of the output electrical power P_{elec}, given the magnet material and generator structure and dimensions [46,47].

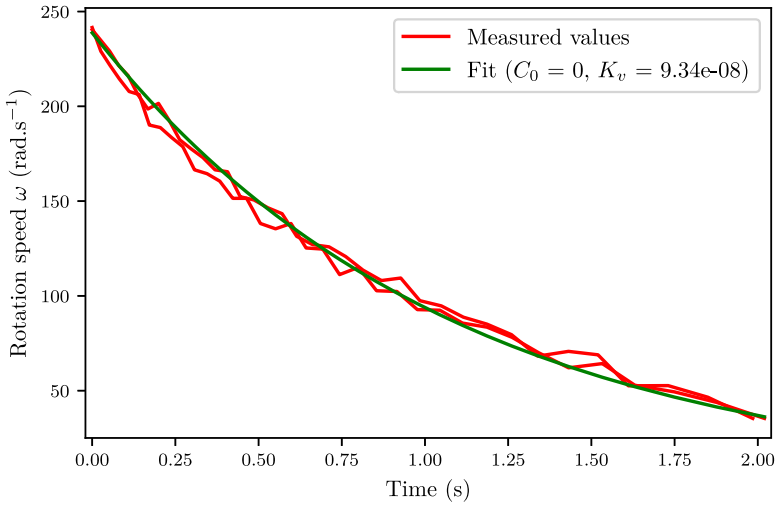

Fig. 10. Decrease of ω and best fit to estimate the losses in the bearings.

Therefore, it is possible to express the total electromagnetic coil losses in the alternator as a function of the output power:

$$P_{coil,J} + P_{coil,E} = \left(\frac{R_{in}}{R_{eq}} + \frac{1}{100}\right) P_{elec} \tag{8}$$

4.3.2. In the bearings

In order to evaluate losses in the bearings, a "let it roll" experiment is described in the literature [20,23,48,49]. It consists in setting the turbine rotor at a given rotation speed ω_0 and releasing it. Its rotation speed ω will go down due to friction until it stops. The friction torque C_f and losses P_b in the bearings can be expressed as:

$$C_f = C_0 + K_v\omega \tag{9}$$

$$P_b = C_f\omega = (C_0 + K_v\omega)\omega \tag{10}$$

Using a least squares optimisation algorithm, the two coefficients C_0 and K_v are found by fitting the decrease of ω as a function of time with the law:

$$\omega(t) = (\omega_0 + \frac{C_0}{K_v}) \exp\left(\frac{-K_v t}{J}\right) - \frac{C_0}{K_v}, \tag{11}$$

where J is the propeller's moment of inertia, which is known thanks to the CAD. Fig. 10 shows the exponential decrease of the rotation speed and the fit, with values of C_0 and K_v.

The value of C_0 is questionable: as this parameter represents the starting torque of the rotor, it seems surprising that it could be zero. Even with very efficient bearings, there will always be a starting torque to overcome. Nevertheless, given the use of this method in the literature and without a better way to measure it, this null value is maintained. Moreover, C_0 is factor of ω and K_v of ω^2: so, if C_0 was in the same order than K_v, the rotation speed being in the range of 30 to 700 rad s^{-1}, the difference on power loss in the bearings would always be less than 3%. Finally, bearings losses are expressed as:

$$P_b = 9.34.10^{-8}\omega^2 \tag{12}$$

Therefore, the higher the rotor rotation speed – and thus wind speed – the higher those losses will be.

4.4. Harvester performance

The value of P_{meca} is evaluated by calculating the sum of output power P_{elec} and the different losses P_b, $P_{coil,E}$ and $P_{coil,J}$. Therefore, the power coefficient C_P is calculated as:

$$C_P = \frac{P_{meca}}{P_{air}} = \frac{P_{elec} + P_b + P_{coil,E} + P_{coil,J}}{P_{air}} \tag{13}$$

Moreover, bearing efficiency η_b and coil efficiency η_{coil} are calculated as follows:

$$\eta_b = \frac{P_{elec} + P_{coil,E} + P_{coil,J}}{P_{meca}} \tag{14}$$

$$\eta_{coil} = \frac{P_{elec}}{P_{elec} + P_{coil,E} + P_{coil,J}} \tag{15}$$

Finally, alternator efficiency η_{gene} is a function of the coil and bearing efficiency:

$$\eta_{gene} = \eta_b\eta_{coil} \tag{16}$$

4.4.1. Choice of the best propeller

Given that three physical parameters on the propeller are variable (α_p, β and N_b), a range of different combinations are tested in order to define the best possible geometry. The only output that is considered here for the improvement is the overall efficiency of the harvester η, with a given propeller. The followed experimental plan is orthogonal: two parameters are fixed while the third changes. Indeed, the three variables are considered independent so their mutual influence is not studied.

The experiments are conducted in the "low speed" wind tunnel, up to 2.3 m s^{-1}. For each propeller, the output power and the overall efficiency are calculated. All the propellers tested have a cut-in speed of 2 m s^{-1}. The cut-in speed is the minimal wind speed at which the rotor of the turbine starts to have a stabilised rotation. When the rotation is launched, by decreasing the airflow slowly step by step, the turbine can continue to run in a stabilised manner at lower wind speeds than the cut-in speed (1.7, 1.4 or even 1.2 m s^{-1}). Fig. 11 presents the results.

First, five propellers are tested, with the coning angle β fixed at 5° and the number of blades N_b at 6 with the pitch angle α_p varies from 8 to 50° (Fig. 11(a)). It can be deduced that the pitch angle giving the highest efficiency of the whole harvester is $\alpha_p = 30°$. The results for $\alpha_p = 20°$ are close, especially at low speeds, and are even slightly better at 1.2 and 1.4 m s^{-1} (0.2% of difference). The coning angle has a lower influence: with $\alpha_p = 30°$ and $N_b = 6$; it can be seen in Fig. 11(b) that the three graphs are almost on top of each other. Nonetheless, it appears that the best choice would be $\beta = 5°$. The effect of the number of blades on output power and efficiency is predictable: the more there is, the better it is. Fig. 11(c) highlights this: with $\alpha_p = 30°$ and $\beta = 5°$, performance is better for $N_b = 8$.

Finally, this leads to an optimal propeller with the following properties: $\alpha_p = 30°$, $\beta = 5°$ and $N_b = 8$. Moreover, it can be noted that this geometry allows the exploitation of the slowest air thanks to the decrease in operating speed to 1.2 m s^{-1}. All results and exploitations presented in the following section are for this chosen propeller.

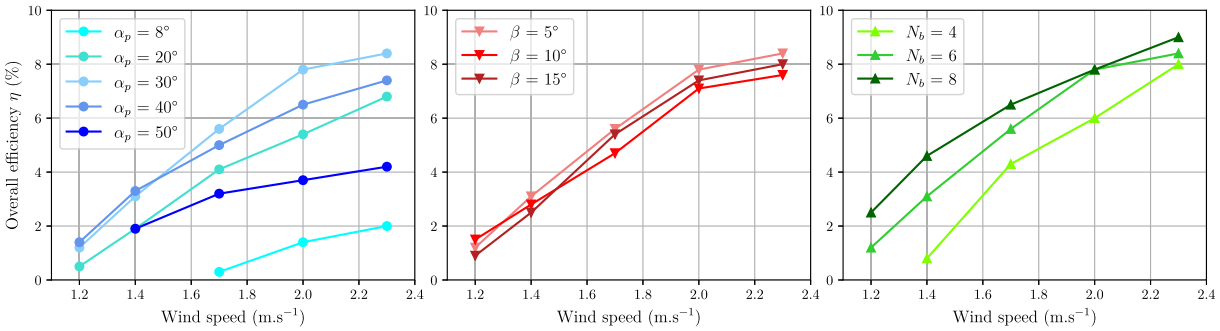

Fig. 11. Influence of propeller geometry on the overall efficiency: variation of (*a*) α_p (with $\beta = 5°$ and $N_b = 6$), (*b*) β (with $\alpha_p = 30°$ and $N_b = 6$) and (*c*) N_b (with $\alpha_p = 30°$ and $\beta = 5°$).

4.4.2. Power production and efficiency

The harvester is tested for airspeeds between 1.2 and 8 m s^{-1}. With the optimal propeller, the cut-in speed is around 2 m s^{-1}, it can produce power until 1.2 m s^{-1} and stops at 1 m s^{-1}.

The output electrical power measured in the resistive load ranges from 41 μW at 1.2 m s^{-1} to 81.7 mW at 8 m s^{-1}. Its evolution is illustrated in Fig. 12(*a*). It is interesting to note that it follows a convex trend without a point of inflexion that would reflect an important drop in efficiency (this phenomenon can be seen in a study by Gasnier et al. between 3 and 3.5 m s^{-1} and between 5 and 7 m s^{-1} [20]). Indeed, with constant efficiency, air power and output power are related to the cube of wind speed as shown in (1) and (2). In other words, the harvester presented here maintains satisfactory efficiency on a large range of wind speeds. Furthermore, in confirmation of the choice of 8 blades, Fig. 12(*b*) presents the output power for the propellers with 4, 6 and 8 blades, and with $\alpha_p = 30°$ and $\beta = 5°$. This comparison can only be made for low air speeds, as the only propeller tested for $U_0 >$ 2.3 m s^{-1} is the optimal one with $N_b = 8$.

In order to analyse wind turbine performance, tip-speed ratio λ is calculated at each wind speed U_0 as the ratio between tangential speed at the tip of the blades V_{tip} and U_0:

$$\lambda = \frac{V_{tip}}{U_0} = \frac{R_r \omega}{U_0} = \frac{R_r 2\pi f}{U_0}, \tag{17}$$

with R_r the radius of the propeller, ω its rotational speed, and f its rotational frequency. The interest of this parameter is that it removes the main scaling effects of size and flow speed, so different wind turbines can be properly compared.

Fig. 13 presents the evolution of the overall efficiency η as a function of the tip-speed ratio, for each wind speed tested. These curves were obtained by setting the wind tunnel to the desired speed, then varying the resistive load connected in parallel of the harvester (from its higher value to the lowest). This modifies turbine rotor speed and thus output power. The same graph with power coefficient as the *y*-axis is given in the discussion in Fig. 16.

The maximum overall efficiency ranges from 2.6% at 1.2 m s^{-1} to 17.4% at 8 m s^{-1}, reaching 17.8% at 4 m s^{-1}. For each wind speed, the optimal value is obtained at different values of λ, from 0.5 to 1.5. Globally, the strongest airflows induce the highest values of η. It can also be noted that the highest rotor frequency ranges from 456 to 7500 rpm at 1.2 and 8 m s^{-1}, respectively, and is obtained for R_{load} close to its maximum.

The overall efficiency can also be plotted as a function of the equivalent resistive load R_{eq} (Fig. 14).

In the first instance, this graph highlights that the resistive load generating optimal efficiency depends on airspeed: it decreases as wind increases. Nevertheless, the optimal loads stay within a reasonable interval, between around 300 and 3000 Ω. Moreover, two "domains" appear: for winds from 1.2 to 2.3 m s^{-1}, the value $R_{eq} = 2000$ Ω gives 88 to 100% of the maximal overall efficiency and thus of the maximal achievable output power. For airspeeds between 3 and 8 m s^{-1}, 85 to 100% of the electrical power is produced with $R_{eq} = 400$ Ω. This shows that the choice of resistive load to make the most of the wind power could be quite simple, with two or three optimal values chosen according to wind speed.

Fig. 15 shows, for each different tunnel speed, the individual efficiencies of the different stages of the harvester at the point of maximum measured output power. The values illustrated are coil efficiency $\eta_{coil} = \eta_{coil,E}\eta_{coil,J}$, bearings efficiency η_b, mechanical-to-electrical conversion efficiency $\eta_{gene} = \eta_b\eta_{coil}$, power coefficient C_P, and finally overall efficiency η.

First, it can be seen that coil efficiency is very interesting, always above 75%, and is higher at low airspeeds. On the contrary, the bearings are moderately efficient at low airspeeds, around 40%, and improve until 8 m s^{-1} to get around 80%. As a consequence, the generator is efficient between less than 40% to 65%.

Moreover, the aerodynamic efficiency of the rotor C_P is much lower but still very correct compared to the literature and the size of the harvester. The smallest value of 7% is obtained at the lowest wind speed, and it goes up to 28.4% at 4 m s^{-1}. Overall wind turbine efficiency begins quite low for 1.2 m s^{-1} at around 3%. Then, it progresses linearly until its maximum of almost 20% at 4 m s^{-1}, and stays approximately at this value for 5 and 8 m s^{-1}.

Overall, the different curves seem to stabilise at optimal values from 4 or 5 m s^{-1}, except for η_{coil} which is lower than at low speeds. It highlights the fact that the harvester finds its best performances at a moderate airspeed, between 4 and 8 m s^{-1}. The explanation of a maximum at 4 m s^{-1} could come from the leading-edge vortices that occurs on samaras wings, as well as on insect wings, and which create a high lift force compared to their wing area [35,45]. Those vortices could also improve the aerodynamical properties of the rotor. The wind speed of 4 m s^{-1} may induce a perfect Reynolds number for the appearance of such particular flows, which then may improve the mechanical power on the turbine shaft.

For details on power values, losses, and efficiencies, all data are listed in Table 5.

5. Discussion

Turbine performance is defined by its overall efficiency but also by its power coefficient. Here, we propose to compare the C_P of our centimetre-scale harvester with that of large scale wind turbines. In his book, Hau gives the evolution of this parameter with tip-speed ratio for various types of wind turbines (for example two-bladed, three-bladed, Savonius...) [50]. With tip-speed ratios measured during our experiments, the type of large scale turbine that has the closest operating area is the "American wind turbine"; it presents more than six blades and a diameter of approximately ten metres. The large number

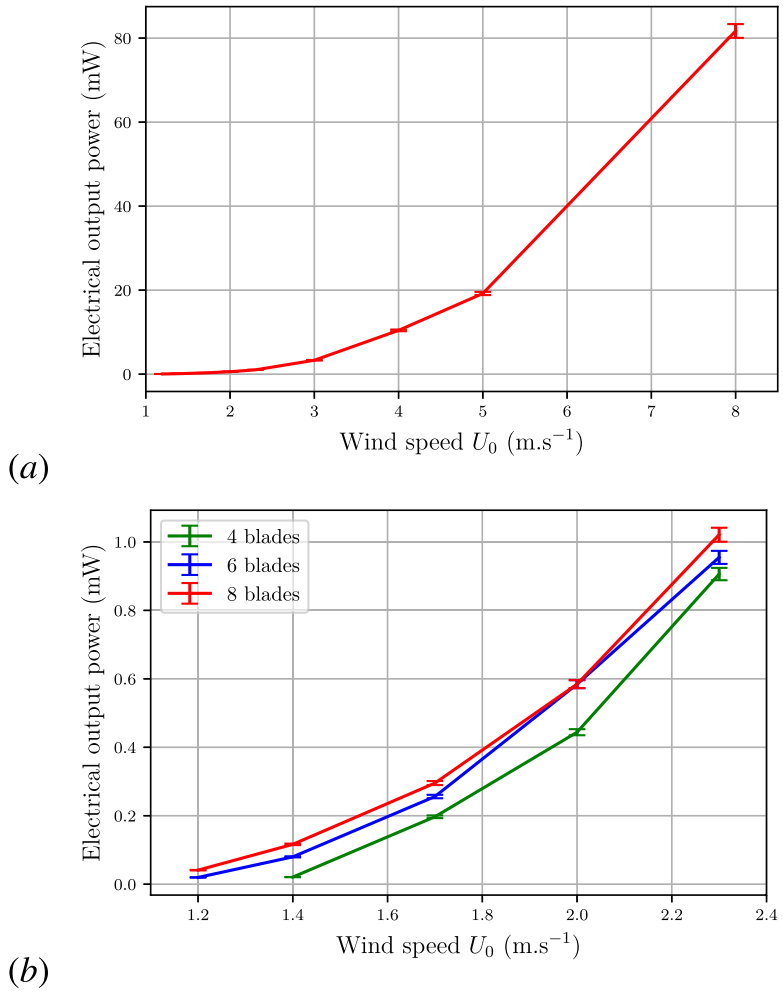

Fig. 12. Maximum output power (*a*) for each wind speed tested for the optimal propeller and (*b*) for wind speeds between 1.2 and 2.3 m s^{-1} for propellers with 4, 6 and 8 blades, $\alpha_p = 30°$ and $\beta = 5°$.

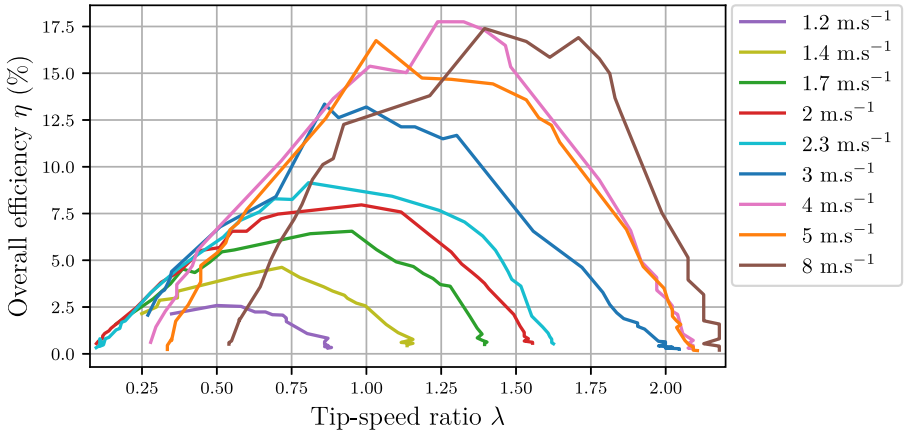

Fig. 13. Overall efficiency as a function of the tip-speed ratio for various wind speeds.

of blades coincides with the optimal value of $N_b = 8$ found earlier. Fig. 16 shows the power coefficient of the bioinspired harvester as a function of λ, for each airspeed tested, as well as the theoretical C_P of Hau's American wind turbine.

The evolution of the C_P for our prototype is relatively independent of airspeed: the different curves follow almost the same trend. They are linearly increasing at low tip-speed ratios, present a maximum value of $\lambda = 1.3$–1.4 and then decrease. The curve at 3 m s^{-1} is surprising because C_P increases until $\lambda = 2$. Compared to the power coefficient of the large scale turbine, it is much lower at low tip-speed ratios: between 5 and 15% against 25%–30%. However, the maximal values are quite close to the value for large scale: between 24 and 29% against 31%, but are reached for a slightly higher tip-speed ratio. This highlights a weakness of the bioinspired propeller: it is not efficient enough at low λ and thus at low rotation speeds. Overall, despite the important gap of scale between the American wind turbine and the harvester presented

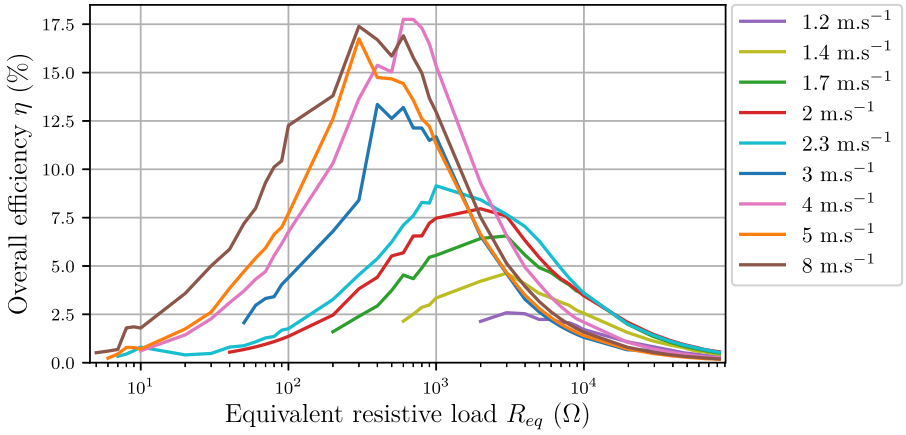

Fig. 14. Overall efficiency as a function of the resistive load for various wind speeds.

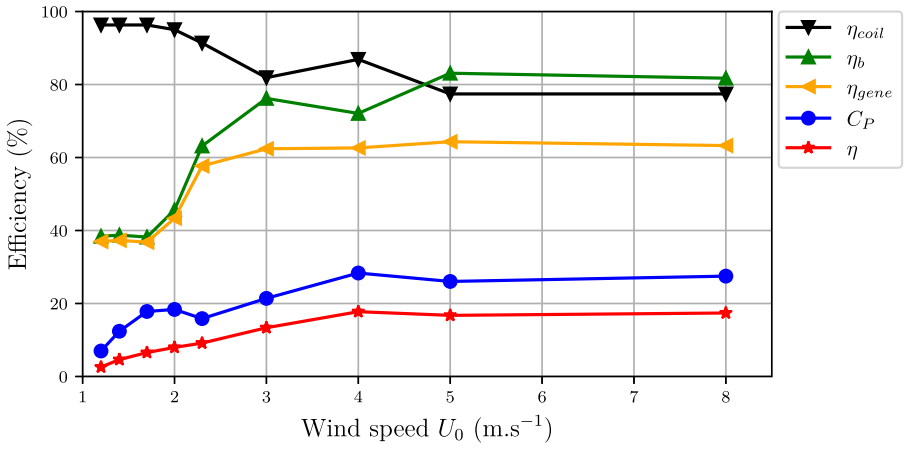

Fig. 15. Evolution of different harvester efficiencies with wind speed, at point of maximum output power.

Table 5
Summary of the powers, losses, and efficiencies for the maximal electrical power at each flow speed tested.

U_0 (m s^{-1})	P_{air} (mW)	P_{meca} (mW)	C_P (%)	P_b (loss) (mW)	η_b (%)	$P_{coil,E}$ (loss) (mW)	$P_{coil,J}$ (loss) (mW)	η_{coil} (%)	max(P_{elec}) (mW)	η (%)
1.2	1.585	0.111	7	0.068	38.4	0.4.10^{-3}	0.001	96.3	0.041	2.6
1.4	2.517	0.312	12.4	0.191	38.7	0.001	0.003	96.3	0.116	4.6
1.7	4.507	0.803	17.8	0.496	38.2	0.003	0.008	96.3	0.295	6.6
2	7.339	1.348	18.4	0.733	45.6	0.006	0.025	95	0.584	8
2.3	11.162	1.770	15.9	0.652	63.1	0.01	0.086	91.4	1.021	9.1
3	24.769	5.302	21.4	1.262	76.2	0.033	0.7	81.9	3.308	13.4
4	58.712	16.643	28.4	4.647	72.1	0.104	1.469	86.9	10.423	17.8
5	114.671	29.857	26	5.048	83.1	0.192	5.411	77.4	19.206	16.8
8	469.693	129.134	27.5	23.599	81.7	0.817	23.019	77.4	81.7	17.4

in this work, their characteristics are quite similar especially at high tip-speed ratios.

It can also be noted that the maximal values of C_P on this graph do not correspond to the values presented in Table 4. Indeed, peaks in the electrical output power occur at tip-speed ratios where C_P can be lower than its maximum; those values of λ are not optimal for the turbine rotor.

Moreover, the performances of the bioinspired harvester are compared to that of the centimetre-scale devices from the literature in Fig. 17. For each miniature wind turbine, the maximum electrical output power density (ratio between P_{elec} and rotor area) is plotted as a function of airspeed. The Betz limit of 59.3% and the upper bound of 30% are also shown. In cases of turbines with a duct, the calculation of power density is based on rotor area rather than on the entire device cross-section, as we consider this to be the best comparison.

In terms of power density – which is directly linked to the overall efficiency – the prototype presented in this work outperforms those in the literature with diameters of 7 cm and less [16–19,21–23], except for the 3.5 cm turbine of Gasnier et al. [20]. Moreover, it covers a larger range of low wind speeds than all the other prototypes, from very low to moderately high, and it maintains good performance throughout. This is partly due to its interesting cut-in speed of 2 m s^{-1} and operating speed down to 1.2 m s^{-1}.

Finally, in terms of WSN supply, the minimum power required for proper node operation is around 100 μW [1]. Our device can harvest enough power for this purpose from a low-speed airflow of 1.4 m s^{-1}.

6. Conclusions

The device presented in this paper is, to the authors' knowledge, the first samara-based wind energy harvester reported to date and one

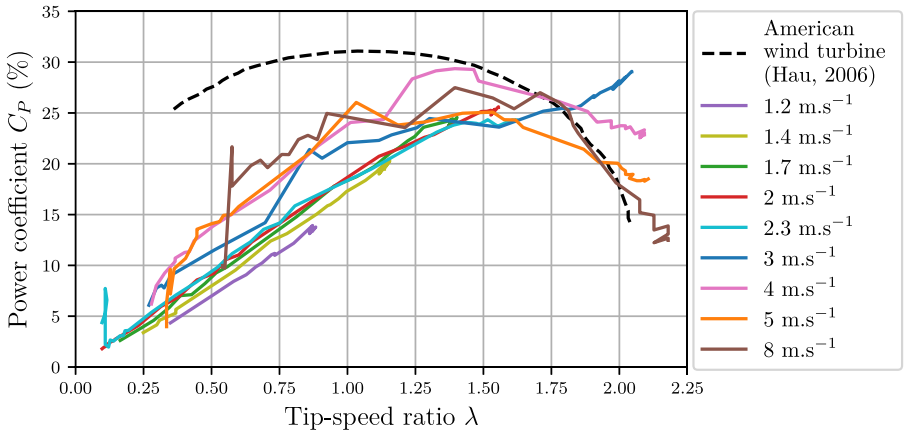

Fig. 16. Comparison of power coefficient values between the bioinspired harvester and the American wind turbine (theoretical) [50].

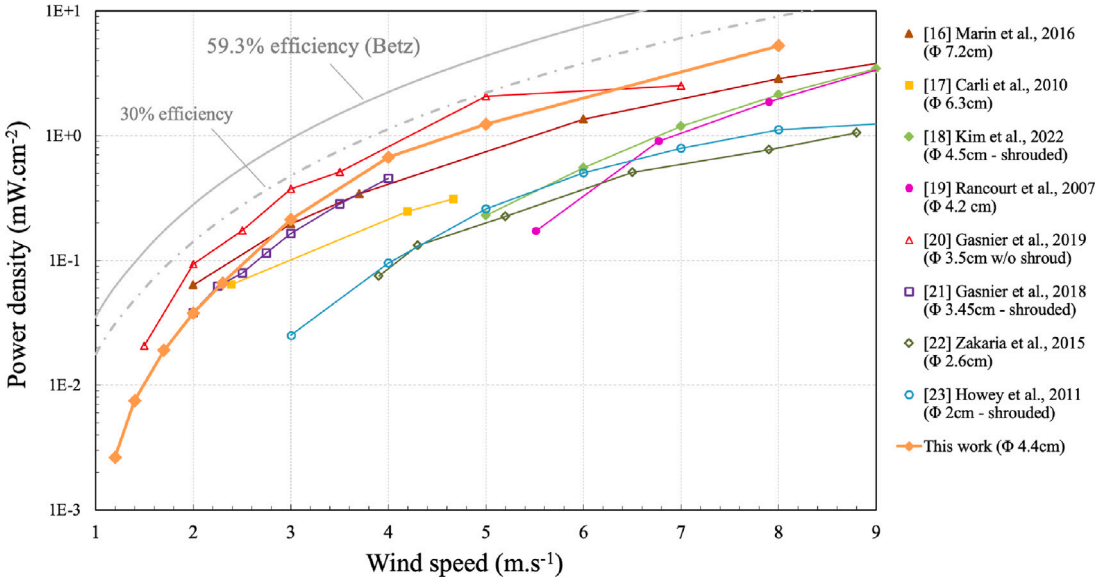

Fig. 17. Power density comparison for centimetre-scale harvesters in the literature (diameter ≤ 7 cm).

of the smallest wind turbines in the literature. The biomimetic design of the propeller is based on the shape of samaras, in particular on the undulation of their wing and on their outer dimensions. This makes it possible to expand the range of wind speeds in which the harvester operates, particularly with low speeds, from 1.2 to 8 m s^{-1}. The output electrical power ranges from 41 μW to 81.7 mW, with an overall efficiency up to 17.8% and a power coefficient up to 28.4%. Overall performance is greater than that of small-scale wind turbines in the literature, except for one. This bioinspired turbine could supply WSNs in difficult-to-access or constrained areas where maintenance cannot be regular and/or batteries cannot be used, or in buildings and houses (hallways, ventilation ducts...).

Nevertheless, some issues and limitations have to be addressed in future works; here some points to consider. First, efficiency: power density and power coefficients are the worst at low wind speeds. One way of improvement could be to dive deeper into the analysis of samara behaviour and structure to make blade design even more specific. The precision of the fabrication process would need to go beyond the present limit of 140 μm, in order to further imitate the maple samara shape. A technological solution to change the pitch angle α_p and the coning angle β during the rotation could also improve rotor efficiency regarding the wind speed. Furthermore, bearing losses are higher at low airspeeds which directly impacts η. The bearings could be improved, or the pivot link completely redesigned. Another way to improve the performances of the generator is to use NdFeB for the magnet instead of SmCo, which presents a higher remanent induction (1.2 T vs 0.9 T) and thus could create a higher current. The generator structure (magnet and coil shapes) could also be modified in order to optimise the magnetic field in the conductor.

CRediT authorship contribution statement

Aurélien Carré: Conceptualization, Methodology, Software, Validation, Investigation, Writing – original draft. **Pierre Gasnier:** Methodology, Investigation, Writing – review & editing. **Émile Roux:** Software, Validation, Supervision, Writing – review & editing. **Laurent Tabourot:** Methodology, Supervision, Writing – review & editing.

Declaration of competing interest

The authors declare that they have no known competing financial interests or personal relationships that could have appeared to influence the work reported in this paper.

Data availability

Data will be made available on request.

References

[1] Huet F. Développement de structures hybrides électromécaniques pour micro-sources d'énergie : générateurs piézoélectriques linéaires et non linéaires (Ph.D. thesis), 2016.

[2] Moschitta A, Neri I. Power consumption assessment in wireless sensor networks. ICT - Energy - Concepts Towards Zero - Power Inform Commun Technol 2014;203–24. http://dx.doi.org/10.5772/57201.

[3] Singh RK, Ahmed MR, Zullah MA, Lee Y-H. Design of a low Reynolds number airfoil for small horizontal axis wind turbines. Renew Energy 2012;42:66–76. http://dx.doi.org/10.1016/j.renene.2011.09.014.

[4] Singh RK, Ahmed MR. Blade design and performance testing of a small wind turbine rotor for low wind speed applications. Renew Energy 2013;50:812–9. http://dx.doi.org/10.1016/j.renene.2012.08.021.

[5] Arroyo A, Manana M, Gomez C, Fernandez I, Delgado F, Zobaa AF. A methodology for the low-cost optimisation of small wind turbine performance. Appl Energy 2013;104:1–9. http://dx.doi.org/10.1016/j.apenergy.2012.10.068.

[6] Bressers S, Avirovik D, Vernieri C, Regan J, Chappell S, Hotze M, et al. Small-scale modular windmill. Am Ceram Soc Bull 2010;89(8):34–40.

[7] Kishore RA, Priya S. Design and experimental verification of a high efficiency small wind energy portable turbine (SWEPT). J Wind Eng Ind Aerodyn 2013;118:12–9. http://dx.doi.org/10.1016/j.jweia.2013.04.009.

[8] Kishore RA, Coudron T, Priya S. Small-scale wind energy portable turbine (SWEPT). J Wind Eng Ind Aerodyn 2013;116:21–31. http://dx.doi.org/10.1016/j.jweia.2013.01.010.

[9] Kishore RA, Marin A, Priya S. Efficient direct-drive small-scale low-speed wind turbine. Energy Harvest Syst 2014;1(1–2):27–43. http://dx.doi.org/10.1515/ehs-2014-0004.

[10] Holmes AS, Hong G, Pullen KR. Axial-flux permanent magnet machines for micropower generation. J Microelectromech Syst 2005;14(1):54–62. http://dx.doi.org/10.1109/JMEMS.2004.839016.

[11] Rivarolo M, Freda A, Traverso A. Test campaign and application of a small-scale ducted wind turbine with analysis of yaw angle influence. Appl Energy 2020;279:115850. http://dx.doi.org/10.1016/j.apenergy.2020.115850.

[12] Rahmatian MA, Tari PH, Mojaddam M, Majidi S. Numerical and experimental study of the ducted diffuser effect on improving the aerodynamic performance of a micro horizontal axis wind turbine. Energy 2022;245:123267. http://dx.doi.org/10.1016/j.energy.2022.123267.

[13] Lipian M, Dobrev I, Massouh F, Jozwik K. Small wind turbine augmentation: Numerical investigations of shrouded- and twin-rotor wind turbines. Energy 2020;201:117588. http://dx.doi.org/10.1016/j.energy.2020.117588.

[14] Dar AS, Barcos GA, Porté-Agel F. An experimental investigation of a roof-mounted horizontal-axis wind turbine in an idealized urban environment. Renew Energy 2022;193:1049–61. http://dx.doi.org/10.1016/j.renene.2022.05.035.

[15] Perez M, Boisseau S, Gasnier P, Willemin J, Geisler M, Reboud J-L. A cm scale electret-based electrostatic wind turbine for low-speed energy harvesting applications. Smart Mater Struct 2016;25(4):045015. http://dx.doi.org/10.1088/0964-1726/25/4/045015.

[16] Marin A, Kishore R, Schaab DA, Vuckovic D, Priya S. Micro wind turbine for powering wireless sensor nodes. Energy Harvest Syst 2016;3(2):139–52. http://dx.doi.org/10.1515/ehs-2013-0004.

[17] Carli D, Brunelli D, Bertozzi D, Benini L. A high-efficiency wind-flow energy harvester using micro turbine. In: SPEEDAM 2010 - International symposium on power electronics, electrical drives, automation and motion. 2010, p. 778–83. http://dx.doi.org/10.1109/SPEEDAM.2010.5542121.

[18] Kim I-H, Kim B-R, Yang Y-J, Jang S-J. Parametric study on ducted micro wind energy harvester. Energies 2022;15(3). http://dx.doi.org/10.3390/en15030727.

[19] Rancourt D, Tabesh A, Fréchette L. Evaluation of centimeter-scale micro windmills: Aerodynamics and electromagnetic power generation. Proc PowerMEMS 2007;93–6.

[20] Gasnier P, Alessandri B, Fayer T, Garraud N, Pauliac-Vaujour E, Boisseau S. Modelling and characterization of a high-efficiency, cm-scale and low velocity airflow-driven harvester for autonomous wireless sensor nodes. Proc PowerMEMS 2019.

[21] Gasnier P, Willemin J, Boisseau S, Goubault De Brugière B, Pillonnet G, Gomez B, et al. A cm-scale, low wind velocity and 250°C-compliant airflow-driven harvester for aeronautic applications. Proc PowerMEMS 2018.

[22] Zakaria MY, Pereira DA, Hajj MR. Experimental investigation and performance modeling of centimeter-scale micro-wind turbine energy harvesters. J Wind Eng Ind Aerodyn 2015;147(September):58–65. http://dx.doi.org/10.1016/j.jweia.2015.09.009.

[23] Howey DA, Bansal A, Holmes AS. Design and performance of a centimetre-scale shrouded wind turbine for energy harvesting. Smart Mater Struct 2011;20(8):085021. http://dx.doi.org/10.1088/0964-1726/20/8/085021.

[24] Kunz PJ. Aerodynamics and design for ultra-low Reynolds number flight (Ph.D. thesis), 2003.

[25] Sunada S, Yasuda T, Yasuda K, Kawachi K. Comparison of wing characteristics at an ultralow Reynolds number. J Aircr 2002;39(2).

[26] Wang YY, Hu WR, Zhang SD. Performance of the bio-inspired leading edge protuberances on a static wing and a pitching wing. J Hydrodyn 2015;26(6):912–20. http://dx.doi.org/10.1016/S1001-6058(14)60100-1.

[27] van Nierop EA, Alben S, Brenner MP. How bumps on whale flippers delay stall: An aerodynamic model. Phys Rev Lett 2008;100:054502. http://dx.doi.org/10.1103/PhysRevLett.100.054502.

[28] Fish FE, Weber PW, Murray MM, Howle LE. The tubercles on humpback whales' flippers: Application of bio-inspired technology. Integr Comp Biol 2011;51(1):203–13. http://dx.doi.org/10.1093/icb/icr016.

[29] Rao C, Ikeda T, Nakata T, Liu H. Owl-inspired leading-edge serrations play a crucial role in aerodynamic force production and sound suppression. Bioinspir Biomim 2017;12(4). http://dx.doi.org/10.1088/1748-3190/aa7013.

[30] Ikeda T, Tanaka H, Yoshimura R, Noda R, Fujii T, Liu H. A robust biomimetic blade design for micro wind turbines. Renew Energy 2018;125:155–65. http://dx.doi.org/10.1016/j.renene.2018.02.093.

[31] Cognet V, Courrech du Pont S, Dobrev I, Massouh F, Thiria B. Bioinspired turbine blades offer new perspectives for wind energy. Proc Royal Soc A 2017;473(2198):20160726. http://dx.doi.org/10.1098/rspa.2016.0726.

[32] Chu Y-J, Lam H-F. Comparative study of the performances of a bio-inspired flexible-bladed wind turbine and a rigid-bladed wind turbine in centimeter-scale. Energy 2020;213:118835. http://dx.doi.org/10.1016/j.energy.2020.118835.

[33] Rosen A, Seter D. Vertical autorotation of a single-winged samara. J Appl Mech 1991;58:1064–71. http://dx.doi.org/10.1115/1.2897683.

[34] Seter D, Rosen A. Study of the vertical autorotation of a single-winged samara. Biol Rev 1992;67:175–97.

[35] Lentink D, Dickson WB, van Leeuwen JL, Dickinson MH. Leading-edge vortices elevate lift of autorotating plant seeds. Science 2009;324:1438–40. http://dx.doi.org/10.1126/science.1174196.

[36] Ulrich ER, Pines DJ, Humbert JS. From falling to flying: The path to powered flight of a robotic samara nano air vehicle. Bioinspir Biomim 2010;5(4). http://dx.doi.org/10.1088/1748-3182/5/4/045009.

[37] Holden JR, Caley TM, Turner MG. Maple seed performance as a wind turbine. 53rd AIAA Aerospace Sciences Meeting 2015;1–14. http://dx.doi.org/10.2514/6.2015-1304.

[38] Carré A, Roux E, Tabourot L, Gasnier P. Innovative blade shape for micro wind turbines. IEEE Wireless Power Week (WPW) 2022;121–5. http://dx.doi.org/10.1109/WPW54272.2022.9854036.

[39] Norberg RA. Autorotation, self stability, and structure of single winged fruits and seeds with comparative remarks on animal flight. Biol Rev 1973;48:561–96. http://dx.doi.org/10.1111/j.1469-185X.1973.tb01569.x.

[40] Nathan R, Katul GG, Horn HS, Thomas SM, Oren R, Avissar R, et al. Mechanisms of long-distance dispersal of seeds by wind. Nature 2002;418(July):409–14. http://dx.doi.org/10.1038/nature00930.1.

[41] Nathan R. Long-distance dispersal of plants. Science 2006;313:786–8. http://dx.doi.org/10.1126/science.1124975.

[42] Green DS. The terminal velocity and dispersal of spinning samaras. Am J Bot 1980;67(8):1218–24. http://dx.doi.org/10.2307/2442364.

[43] Nave GK, Hall N, Somers K, Davis B, Gruszewski H, Powers C, et al. Wind dispersal of natural and biomimetic maple samaras. Biomimetics 2021;6(2). http://dx.doi.org/10.3390/biomimetics6020023.

[44] Yasuda K, Azuma A. The autorotation boundary in the flight of samaras. J Theoret Biol 1997;185:313–20. http://dx.doi.org/10.1006/jtbi.1996.0299.

[45] Levy D-E, Seifert A. Parameter study of simplified dragonfly airfoil geometry at Reynolds number of 6000. J Theoret Biol 2010;266:691–702. http://dx.doi.org/10.1016/j.jtbi.2010.07.016.

[46] Wu W, Dunlop JB, Collocott SJ. Modelling of eddy-current losses in a surface-mounted NdFeB permanent-magnet generator. Proceedings of the Seventeenth International Workshop on Rare-earth Magnets and Applications 2002;323–8.

[47] Wang R-J, Kamper MJ. Calculation of eddy current loss in axial field permanent-magnet machine with coreless stator. IEEE Trans Energy Convers 2004;19(3):532–8. http://dx.doi.org/10.1109/TEC.2004.832043.

[48] Gasnier P, Saoutieff E, Soriano O, Alessandri B, Ojer-Aranguren J, Boisseau S. Cm-scale axial flow water turbines for autonomous flowmeters: An experimental study. Smart Mater Struct 2018;27. http://dx.doi.org/10.1088/1361-665X/aae774.

[49] Mungan CE. Frictional torque on a rotating disc. Eur J Phys 2012;33:1119–23. http://dx.doi.org/10.1088/0143-0807/33/5/1119.

[50] Hau E. Wind turbines. 2006.